Recent advances in using Chinese Earth observation satellites for remote sensing of vegetation

Zhengyang Zhang[1], Lei Lu[1], Yuhe Zhao[1], Yuanyuan Wang[2], Dandan Wei[3], Xiaodan Wu[1], Xuanlong Ma[1,*]

[1] College of Earth and Environmental Sciences, Lanzhou University, Lanzhou, Gansu, 730000 China

[2] National Satellite Meteorological Centre, China Meteorological Administration, Beijing, 100082 China

[3] Land Satellite Remote Sensing Application Center, Ministry of Natural Resources, Beijing, 10048, China

* correspondence to: X.Ma., Tianshuinan Road 222, Lanzhou, China, 730000 (xlma@lzu.edu.cn)

Abstract

Vegetation is an important component of the Earth system as it supports other terrestrial biological activities through the photosynthetic production. The biophysical and biochemical parameters of vegetation retrieved from satellite observations have been used extensively in global vegetation monitoring and Earth system modeling. So far, most of vegetation remote sensing applications used data from sensors onboard satellites from American or European space agencies. From the user perspective, it would be beneficial to have an even more diverse data sources that can secure data sustainability in case of satellite retirement or sensor failure and enables research opportunities such as multi-sensor data fusion/integration and multi-angle remote sensing. In this regard, it would be worth exploring the potential of the Chinese Earth Observation Satellites (CEOS) for monitoring vegetation dynamics and for understanding Earth system functioning in general from space. Here we summarized the recent advances in applying CEOS data to retrieve several key vegetation parameters widely used in geoscience field. We focused on the uncertainty and limitations by critically examining the case studies conducted over different vegetation types. Suggestions for research opportunities that can benefit from the combined use of data from the CEOSs as well as other international spaceborne sensors are also provided. The hope is to provide the community an overview of what could be useful to their specific geoscientific, environmental and global change studies by leveraging the growing data volume from the orbiting and the planned CEOS sensors.

Keywords: remote sensing of vegetation, Earth system dynamics, global change, multi-sensor fusion, data continuity

1 Introduction

Vegetation remote sensing refers to the retrieval of biochemical and biophysical parameters of vegetation using satellite observations (Aplin 2005). Commonly used vegetation parameters include vegetation indices (VIs), leaf area index (LAI), fractional vegetation cover (FVC), aboveground biomass (AGB) and sun-induced chlorophyll fluorescence (SIF) (Cohen and Goward 2004; Kerr and Ostrovsky 2003; Wulder et al. 2004). These parameters have been widely used as a diagnostic proxy as well as inputs to prediction models in the fields of geoscience, agriculture, ecology, environmental science, and global change (Gianelle et al. 2009; Nara and Sawada 2021; Pettorelli et al. 2005).

Over past few decades, the field of remote sensing of vegetation witnessed rapid advances and enormous successes. A large credit should be given to the significant amount of investment, usually from state governments, to the satellite sensors that eventually enabled global monitoring of vegetation dynamics and associated geoscientific applications. Spaceborne sensors such as AVHRR (Advanced Very-High-Resolution Radiometer), MODIS (Moderate-resolution Imaging Spectroradiometer) and ETM+ (Enhanced Thematic Mapper plus), have acquired a huge amount of science-quality data that led to a surge of applications in vegetation remote sensing (Davis et al. 2017; Liu et al. 2018; Mancino et al. 2020; Zhang et al. 2017; Zhou et al. 2018; Zoungrana et al. 2018).

Deleted:

Recently, China has started launching more and more Earth Observation satellites that carry instruments including multispectral, hyperspectral sensors and Synthetic Aperture Rader (SAR), in together termed as the Chinese Earth Observation Satellites (CEOSs) (Figure 1). There have been many studies using data from CEOSs for retrieving vegetation parameters. A systemic review on the potential and limitations of the sensors onboard CEOSs for remote sensing of vegetation, however, is not available yet. To what extent do the CEOS sensors specifications and performance resemble the industry-standard sensors such as MODIS or ETM+/OLI? What are the accuracies for retrieving several commonly-used vegetation parameters from the CEOS sensors in different ecosystem types? What multi-sensor research opportunities are enabled by adding CEOSs? Answering these questions would be useful for the end-users to better use the data from CEOSs in their specific studies. This review aims to provide the community a summary of the recent advances in using CEOS sensors for vegetation remote sensing and its associated applications. To make this review reach a broader international community, most of the literature cited in this review are published in English journals, with the remaining published in Chinese journals at least contain abstracts written in English. In addition, the weblinks to the data portals of CEOSs with English language support are also provided.

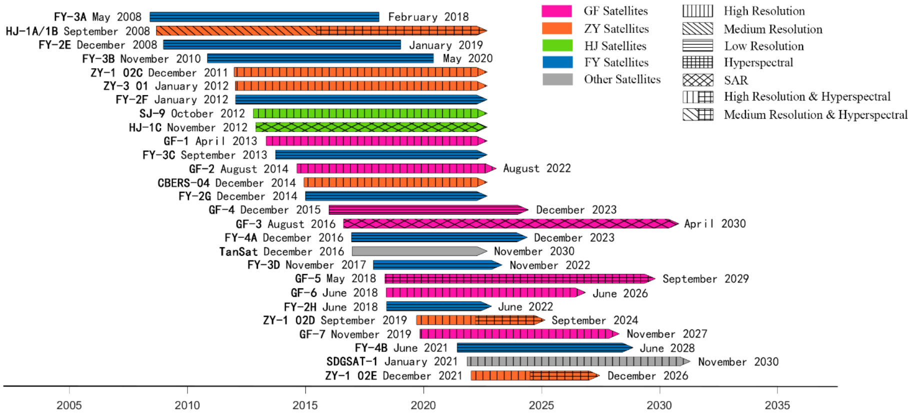

Figure 1 Timelines of several major CEOSs (FY: FengYun Meteorological Satellites; GF: GaoFen Satellites; ZY: ZiYuan Satellites; HJ: HuanJing satellites; SJ: ShiJian satellites; SDGSAT: Sustainable Development Goals Satellite; TanSat: Global CO_2 observation and monitoring satellite)

2 Overview on specifications of the CEOS sensors

At present, there are five major CEOS constellations that have the potential to be used for vegetation remote sensing, including GaoFen, HuanJing/ShiJian, ZiYuan, FengYun and TanSat. Sensors onboard these satellites include panchromatic, visible, multispectral, hyperspectral to Synthetic Aperture Radar (SAR), with data recorded at different spatial resolutions (submeter to kilometer). Table 1 summarizes the specifications of above five CEOS constellations and Figure 2 compares the spectral band configurations between the optical sensors onboard CEOSs and other international satellites.

Deleted: s

Commented [张1]: Table 1 is the specifications of GF satellites.

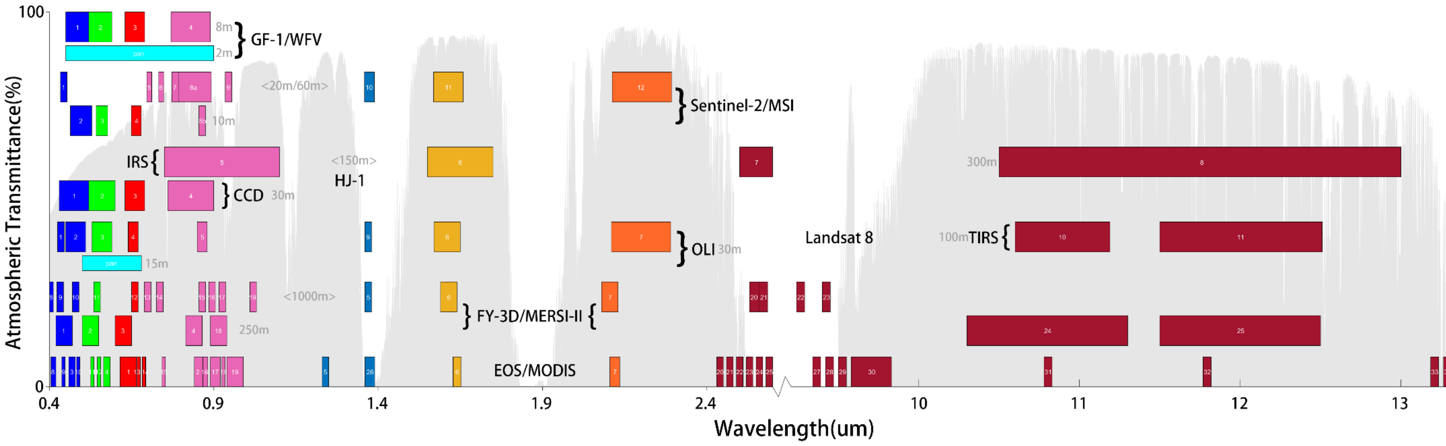

Figure 2 Comparisons in spectral band configurations between optical sensors onboard the CEOSs and other international satellites. Each bar represents a single band the width of the bar indicates bandwidth. The number on the bar indicates the band number. Spatial resolution of each band is indicated with grey-colour text. The background shows the atmospheric transmittance of the 1976 U.S. standard atmosphere.

2.1 GaoFen Satellites

GaoFen (GF in acronym, or “High-resolution”) is a series of Chinese high-resolution Earth imaging satellites, which is part of the state-sponsored Chinese High-resolution Earth Observation System (CHEOS) program. GF-1 is the first satellite of GF series, and was launched on April 26, 2013, with an expected lifetime of 5-8 years. It carries 4 Wide-Field View multispectral sensors (WFV) with 16 m resolution, and a Panchromatic / Multispectral sensor (PMS) with 2 m spatial resolution in panchromatic mode and 8 m spatial resolution in multispectral mode. To date, there have been four nearly identical GF-1 launched into orbits, all can provide high spatial and temporal resolution multispectral measurements. GaoFen-6 (GF-6) is another multispectral satellite launched on June 2, 2018, with an expected lifetime of 8 years. Equipped with the WFV and PMS sensors similar to GF-1, GF-6 also adds a "red edge" band to capture the unique spectral characteristics of crops. GF-1/6 WFV and PMS sensors are similar to Sentinel-2/MSI and SPOT-6(7)/NAOMI, respectively (Appendix Table A1 and A2).

Deleted: designing life

Deleted: a design life

GaoFen-2 (GF-2) was launched on August 19, 2014, with an expected lifetime of 5-8 years. It carries a PMS with the spatial resolution of 0.8 m in panchromatic mode and 3.2 m in multispectral mode, and is the first Chinese sub-meter spatial resolution satellite (Huang et al. 2018; Pan 2015). GF-2/PMS is similar to QuickBird and WorldView satellites (Appendix Table A3).

Deleted: a designing life

GaoFen-3 (GF-3) is a SAR constellation consisting of three satellites, i.e. GF-3 01, GF-3 02 and GF-3 03, that were launched on August 9, 2016, November 22, 2021, and April 7, 2022, respectively. Each of the GF-3 carries the C-band multi-polarization SAR that has the world's largest number of imaging modes with multiple spatial resolutions ranging from 1 m to 500 m and daily temporal resolution. GF-3 is similar to ESA's Sentinel-1 (Appendix Table A4).

GaoFen-4 (GF-4) was launched on December 29, 2015, with an expected lifetime of 8 years. GF-4 is the world's highest spatial resolution geostationary satellite equipped with a 5-channel PMS camera which has a spatial resolution of 50 m (in staring mode). The spectral range of PMS is located between visible and near-infrared. In addition, GF-4 also has a one-channel mid-infrared camera with a spatial resolution of 400 m. GF-4/PMS is similar to GOES-R/ABI and Himawari-8/AHI.

Deleted: a designing life

GaoFen-5 (GF-5) are mainly used as a full-spectrum hyperspectral satellites launched on May 9, 2018 (GF-5 01), and July 9, 2021 (GF-5 02), with an expected lifetime of 8 years. Each of GF-5 satellite carries the Advanced Hyperspectral Imager (AHSI) that has 330 bands from 400 – 2500 nm with a spatial resolution of 30 m. GF-5/AHSI is similar to EO-1/Hyperion and DLR/DESIS (Appendix Table A5).

Deleted: is

Deleted: a design life

Deleted: It

GaoFen-7 (GF-7), launched on November 3, 2019, is mainly used as a high spatial resolution stereo mapping satellite. GF-7 breakthrough the sub-meter stereo mapping technology, and can acquire satellite stereo maps with a scale of 1:10,000.

Table 1 Specifications of the sensors onboard the GF satellites

Satellite	Payload

		Band No.	Spectral Range (μm)	Spatial Resolution (m)	Swath Width (km)	Revisit Cycle (days)	Similar Sensors
GF-1	Panchromatic & Multispectral Camera (PMS)	pan	0.45~0.90	2	60 (2 Cameras)	4	SPOT-6(7)/ NAOMI
		1	0.45~0.52	8			
		2	0.52~0.59				
		3	0.63~0.69				
		4	0.77~0.89				
	Wide-Field View Multispectral Camera (WFV)	5	0.45~0.52	16	800 (4 Cameras)	2	Sentinel-2/ MSI
		6	0.52~0.59				
		7	0.63~0.69				
		8	0.77~0.89				
GF-2	PMS	pan	0.45~0.90	1	45 (2 Cameras)	5	WorldView-3/WV110
		1	0.45~0.52	4			
		2	0.52~0.59				
		3	0.63~0.69				
		4	0.77~0.89				
GF-3	Synthetic Aperture Radar (SAR)	-	C-band: 4-8 GHz	1-500	5-650	Single Vision: <3d; Double Vision: <1.5d	Sentinel-1
GF-4	PMS	pan	0.45~0.90	50	500	20 Seconds	GOES-R/ABI & Himawari-8/AHI
		1	0.45~0.52				
		2	0.52~0.60				
		3	0.63~0.69				
		4	0.76~0.90				
	Infrared Multispectral Camera (IRS)	5	3.50~4.10	400	400		
GF-5	Advanced Hyperspectral Imager (AHSI)	1-300	0.40~2.50	-	60	5	DLR & PRISMA
	Visible and Infrared Multispectral	1	0.45~0.52	20			Sentinel-2/ MSI
		2	0.52~0.60				
		3	0.62~0.68				
		4	0.76~0.86				

Deleted:

Deleted:

Deleted:

Deleted: ;

	Imager (VIMI)	5	1.55~1.75				
		6	2.08~2.35				
		7	3.50~3.90	40			
		8	4.85~5.05				
		9	8.01~8.39				
		10	8.42~8.83				
		11	10.3~11.3				
		12	11.4~12.5				
GF-6	PMS	Same as GF-1/PMS			90 (2 Cameras)	4	Same as GF-1
	WFV	1	0.45~0.52	16	800 (4 Cameras)	2	
		2	0.52~0.59				
		3	0.63~0.69				
		4	0.77~0.89				
		5	0.69~0.73				
		6	0.73~0.77				
		7	0.40~0.45				
		8	0.59~0.63				
GF-7	Bi-linear Array Stereo Mapping Camera	pan	0.45~0.90	0.8	20	5	SPOT-6(7)/ NAOMI
		1	0.45~0.52	3.2			
		2	0.52~0.59				
		3	0.63~0.69				
		4	0.77~0.89				
	Laser Altimeter	-					

2.2 ZiYuan satellites

ZiYuan (ZY in acronym, or "Resources") represents a series of Chinese Earth resource satellites that so far has ZY-1, ZY-2 and ZY-3 in orbits. There are two types of ZY-1 satellites. The first one, ZY-1 01, 02, 02B and 04 satellites, which were made jointly by China and Brazil, is also called China-Brazil Earth Resource Satellite (CBERS). At present, there is only ZY-04 (CBERS-04) operating which was launched on December 7, 2014, with an expected lifetime of 3 years. The other type of ZY-1 includes ZY-1 02C and 02D and 02E satellites were made in China, and were launched on December 22, 2011, September 12, 2019, and December 26, 2021, respectively, all in orbits now. Detail parameters of ZY-1 satellites can be seen in Table 2.

Deleted: a designing life

ZiYuan-3 (ZY-3) is the first civilian high-resolution optical stereo mapping satellite of China (Li 2012; Tang and Hu 2018; Wang et al. 2014a). ZY-3 01 and 02 satellites were launched on January 9, 2012, and May 30, 2016, respectively, forming a constellation with an expected lifetime of 5 years. Each of the ZY-3 satellite carries a nadir-viewing panchromatic TDI (Time Delayed and Integration) CCD camera with a resolution of 2.1 m, two forward-looking and backward-looking panchromatic TDI CCD cameras with a resolution of 3.5 m (ZY-3 01) or 2.5 m (ZY-3 02), and a nadir-viewing multispectral camera with a resolution of 5.8 m. ZY-3 can capture images with seamless coverage between 84°N and 84°S by side-swinging and can obtain images with global coverage every 59 days, forming global long-term 2.1 m resolution stereo images and 6 m multispectral images. ZY-3 also carries a multispectral camera (MUX) which is similar to GF-1/PMS.

Deleted: a design life

Deleted: The

Deleted: of ZY-3

Table 2 Specifications of the sensors onboard ZY satellites

Satellite	Payload	Band No.	Spectral Range (μm)	Spatial Resolution (m)	Swath Width (km)	Revisit Cycle (days)	Similar Sensors
CBERS-04	Panchromatic & Multispectral Camera (PMS)	pan	0.51~0.85	5	60	3	-
		1	0.52~0.59	10			
		2	0.63~0.69				

		3	0.77~0.89				
	Multispectral Camera (MUX)	1	0.45~0.52	20	120	26	
		2	0.52~0.59				
		3	0.63~0.69				
		4	0.77~0.89				
	Infrared Scanner (IRS)	1	0.50~0.90	40	120	26	
		2	1.55~1.75				
		3	2.08~2.35				
		4	10.4~12.5	80			
	Wide-Field Imager (WFI)	1	0.45~0.52	73	866	3	
		2	0.52~0.59				
		3	0.63~0.69				
		4	0.77~0.89				
ZY-1 02C	Panchromatic & Multispectral Camera (PMS)	pan	0.51~0.85	5	60	3	-
		1	0.52~0.59	10			
		2	0.63~0.69				
		3	0.77~0.89				
	High Resolution Camera (HR)	pan	0.50~0.80	2.36	54		
ZY-1 02 D/E	Visible and Near-Infrared Camera (VNIC)	pan	0.452~0.902	2.5	115	3	-
		1	0.452~0.521	10			
		2	0.522~0.607				
		3	0.635~0.694				
		4	0.776~0.895				
		5	0.416~0.452				
		6	0.591~0.633				
		7	0.708~0.752				
		8	0.871~1.047				
	Advanced Hyperspectral Imager (AHSI)	1-166	0.40~2.50	30	60		
ZY-3	CCD Forward	1	0.50~0.80	3.5	52	5	SPOT-6(7)/ NAOMI
	CCD Backward						
	CCD Nadir			2.1	51		
		1	0.45~0.52	6	51	3-5	

	Multispectral Camera (MUX)		2	0.52~0.59				
			3	0.63~0.69				
			4	0.77~0.89				
ZY-3 02	CCD	Forward-looking Camera	1	0.50~0.80	2.5	51	3~5	
		Backward-looking Camera						
		Nadir Camera			2.1			
	Multispectral Camera (MUX)		1	0.45~0.52	5.8	51	3	IKONOS/MS
			2	0.52~0.59				
			3	0.63~0.69				
			4	0.77~0.89				

2.3 HuanJing/ShiJian satellites

HuanJing/ShiJian satellites include HuanJing-1 satellites (HJ-1 in acronym, or "Environment") and ShiJian-9 (SJ-9 in acronym, or "Experiment"), are the Earth observation constellations for environment and nature disasters.

HJ-1 satellites, including two optical satellites HJ-1A and HJ-1B, and one radar satellite, HJ-1C, are operated by the Chinese Centre for Resources Satellite Data and Application (CRESDA). HJ-1A and 1B were launched on September 6, 2008, simultaneously. HJ-1A carries a 30 m resolution CCD camera and a 100 m resolution hyperspectral Imager (HSI), while the HJ-1B satellite carries a 30 m resolution CCD camera and a 150 m resolution Infrared Scanner (IRS). All of the three HJ-1 satellites have an expected lifetime of 3 years, and are still functioning in orbits. HJ-1/HSI and IRS are similar to EO-1/Hyperion and Landsat-8/TIRS, respectively.

Deleted: a design life

SJ-9A/B satellites were launched on December 14, 2012, with an expected lifetime of 3 years. Equipped with PMS and IRS cameras, SJ-9 can acquire VNIR multispectral images and infrared images with 2.5 m and 10 m spatial resolution, respectively.

Deleted: a designing life

Table 3 Specifications of the sensors onboard HJ and SJ satellites

Satellite	Payload	Band No.	Spectral Range (μm)	Spatial Resolution (m)	Swath Width (km)	Revisit Cycle (days)	Similar Sensors
HJ-1A	CCD Scanner	1	0.43~0.52	30	360(Single)700(Parallel)	4	Landsat Series
		2	0.52~0.60				
		3	0.63~0.69				
		4	0.76~0.9				
	Hyperspectral Imager (HSI)	-	0.45~0.95(110-128 bands)	100	50	4	
HJ-1B	CCD Scanner	1	0.43~0.52	30	360 (Single) 700 (Parallel)	4	
		2	0.52~0.60				
		3	0.63~0.69				
		4	0.76~0.90				
	Infrared Scanner (IRS)	5	0.75~1.10	150	720	4	
		6	1.55~1.75				
		7	3.50~3.90				
		8	10.5~12.5	300			
SJ-9A	Panchromatic & Multispectral Camera (PMS)	pan	0.45~0.89	2.5	30	4	-
		1	0.45~0.52	10			
		2	0.52~0.59				
		3	0.63~0.69				
		4	0.77~0.89				

SJ-9B	Infrared Scanner (IRS)	1	0.80~1.20	73	18	8

2.4 FengYun Satellites

The FengYun (FY in acronym, or “Wind and Cloud”) satellites are operated by the Chinese National Satellite Meteorological Center (NSMC). The naming convention for FY satellites is that the odd number represents the polar-orbiting while the even number represents the geostationary. FY-3 is the second generation of the Chinese polar-orbiting meteorological satellites. FY-3A and FY-3B, launched on May 27, 2008 and November 5, 2011, respectively, are the first two that carry a Visible and Infra-Red Radiometer (VIRR) and a Medium Resolution Spectral Imager (MERSI), among other sensors for atmospheric remote sensing (Dong et al. 2009; Zhang et al. 2015). FY-3C, launched on September 23, 2013, is the first operational satellite of FY-3 constellation and carries a MERSI same as FY-3A/FY-3B. FY-3D was launched on November 15, 2017 with an upgraded second generation MERSI instrument (MERSI-II) onboard (Wang et al. 2019). The MERSI-II has a better infrared sensing ability than the MERSI by dividing the original wide infrared spectral channel into six narrow mid- and thermal infrared channels. In addition, MERSI-II also adds the shortwave infrared channel (1.38 μm) and the onboard calibration instrument for the cirrus detection and calibration. FY-3/VIRR is similar to NOAA/AVHRR while MERSI is similar to EOS/MODIS and NPP/VIIRS.

Deleted: and

Deleted: , launched on September 23, 2013 and

Deleted: , respectively, carry

Table 4 Specifications of the sensors onboard FY-3 satellites

Satellite	Payload	Similar Sensors

		Band No.	Spectral Range (μm)	Spatial Resolution (m)	Swath Width (km)	Revisit Cycle ($days$)	
FY-3C	Visible and Infra-Red Radiometer (VIRR)	1	0.58-0.68	1000	2800	5.5	NOAA/AVHRR
		2	0.84-0.89				
		3	3.55-3.93				
		4	10.3-11.3				
		5	11.5-12.5				
		6	1.55-1.64				
		7	0.43-0.48				
		8	0.48-0.53				
		9	0.53-0.58				
		10	1.325-1.395				
	Medium Resolution Spectral Imager (MERSI)	1	0.42~0.52	250	2800	5.5	MODIS & VIIRS
		2	0.5~0.6				
		3	0.6~0.7				
		4	0.815~0.915				
		5	8.75~13.75				
		6	0.392~0.432	1000			
		7	0.423~0.463				
		8	0.47~0.51				
		9	0.5~0.54				
		10	0.545~0.585				
		11	0.63~0.67				
		12	0.665~0.705				
		13	0.745~0.785				
		14	0.845~0.885				
		15	0.885~0.925				
		16	0.92~0.96				
		17	0.96~1				
		18	1.01~1.05				
		19	1.59~1.69				
		20	2.08~2.18				
FY-3D	Medium Resolution Spectral Imager-Ⅱ (MERSI-Ⅱ)	1	0.402~0.422	1000	2800	5.5	MODIS & VIIRS
		2	0.433~0.453				
		3	0.445~0.495	250			
		4	0.48~0.5	1000			
		5	0.525~0.575	250			

Deleted: MERIS

Deleted: MERIS

6	0.545~0.565	1000
7	0.625~0.675	250
8	0.66~0.68	
9	0.699~0.719	1000
10	0.736~0.756	
11	0.855~0.875	
12	0.84~0.89	250
13	0.895~0.915	
14	0.926~0.946	
15	0.915~0.965	
16	1.23~1.31	
17	1.365~1.395	
18	1.615~1.665	1000
19	2.105~2.155	
20	2.99~3.17	
21	3.9725~4.1275	
22	6.95~7.45	
23	8.4~8.7	
24	10.3~11.3	250
25	11.5~12.5	

2.5 TanSat

The Chinese Carbon Dioxide Observation Satellite named as TanSat (or "Carbon Satellite"), launched on December 22, 2016, is the third satellite for global CO_2 monitoring with an expected lifetime of 3 years. TanSat operates in the Sun-synchronous orbit with an orbit period of 98.89 minutes. Equipped with the Atmospheric Carbon-dioxide Grating Spectroradiometer (ACGS), TanSat can capture weak filling effect of the dark Fraunhofer line at Fe (758 nm) and KI (771 nm) from solar-induced chlorophyll fluorescence (SIF) emitted by photosynthetically active land vegetation. Hence, TanSat can not only dynamically monitor the global CO_2 in the atmosphere, but also retrieve SIF precisely. SIF, combined with simultaneous atmospheric CO_2 concentration data,

Deleted: a designing life

Deleted: has the ability to

can accurately estimate global vegetation photosynthetic productivity, which contributes greatly to the global carbon cycle monitoring. Apart from ACGS, TanSat also carries the Cloud Aerosol Polarization Imager (CAPI), which can measure information such as clouds and atmospheric particulate, leading to more accurate CO_2 concentration retrieval (Liu et al. 2018; Zhang et al. 2018; Ran et al. 2019; Ji et al. 2019). TanSat is similar to GOSAT/TANSO-FTS, OCO-2, Sentinel-5P/TROPOMI and FLEX/FLORIS that will be launched in 2025 (Appendix Table A6).

Data derived from GF, ZY, HJ satellites are available at China Centre For Resources Satellite Data and Application (http://www.cresda.com/EN/), and FY and TanSat data are available at National Satellite Meteorological Center (NMSC) (http://www.nsmc.org.cn/nsmc/en/home/index.html). All data accessing platforms are featured with English language support.

3 Retrieval of vegetation parameters using CEOS sensors

3.1 Vegetation Index

Vegetation indices (VIs) such as normalized difference vegetation index (NDVI) are simple and effective parameters used to characterize vegetation cover and growth using remote sensing technique (Bannari et al. 1995; Kalaitzidis et al. 2010; Pettorelli 2013). With a spatial resolution as high as 16 m, VIs derived from GF-1/WFV provided enough spatial details for mapping vegetation in heterogeneous landscapes such as mountain areas (Zhao et al. 2019, 2020). Zhao et al. (Zhao et al. 2013) and Yuan et al. (Yuan et al. 2015) analyzed the relationships of several commonly used vegetation indices (i.e. NDVI, SAVI, and EVI) derived from HJ-1/CCD and Landsat-5/TM or

Deleted: sink

Deleted: observation

Deleted: and support scientists get rid of the interference in the retrieving

Commented [MX2]: SJ 呢？

Commented [MX3]: 不是这么引的，统一改成 Zhao et al. (2013)

譬如这句话就要改成 Zhao et al. (2013) and Yuan et al. (2015) analyzed …. 文中其它做类似修改。

Landsat-7/ETM+, and found that there was a significant positive correlation for all indices among different sensors ($R^2 > 0.90$). Specifically, HJ-1/CCD NDVI is higher than Landsat NDVI in areas with sparse vegetation cover, while the opposite is true in areas with high vegetation cover. This can be attributed to the fact that the upper limit of the spectral range in the red band and the lower limit of the spectral range in the NIR band of HJ-1/CCD are in the range of 0.70~0.75 μm, which generally has smaller reflectance than the Spectral Response Function (SRF) of red and NIR band not cross the range used by, leading to smaller HJ-1/CCD NDVI for densely vegetated areas. Due to the spectral similarity of the bands, Chen et al. (2015) established conversion equations between HJ-1/CCD and EOS/MODIS NDVI, offering the potential for multi-sensor data fusion.

Deleted: It

Deleted: well

Deleted: good

Deleted: NDVI

Wu et al. (2011) analyzed the relationship between FY-3A/MERSI and Terra/MODIS VIs and further verified them using ground VI measurements. The results showed that Terra/MODIS VIs had a higher correlation with field data than FY-3A/MERSI VIs, which was attributed to the broader FY-3A/MERSI bandwidth that was more sensitive to atmospheric influences. Ge et al. (2007) found a strong correlation between FY-3A/MERSI and Terra/MODIS VIs (R = 0.99), and further confirmed the sensitivity of MERSI reflectance to atmospheric water vapor content based on the MODTRAN atmospheric radiative transfer model simulation, especially when water vapor content was greater than $5g/cm^2$.

Deleted: on

Deleted:

Deleted: MODTRAN

There are also several studies that utilized time series VIs derived from CEOS sensors to study vegetation phenology (Li et al. 2017; Yang et al. 2017; Wang et al. 2014). For instance, Song et al. (2018) extracted phenological information from double-cropping rice using 30 m HJ-1/CCD data

Deleted: -

and well revealed the growth of sub-field rice. Li et al. (2019) used HJ-1/CCD data to study forest phenology, and analyzed the response of tree phenology to meteorological forcing.

3.2 Fractional Vegetation Cover

Fractional Vegetation Cover (FVC) is expressed as a percentage of the vertical projected area of vegetation (including stems, leaves, and branches) to the ground area (Gitelson et al. 2002), which is widely used in land degradation research and also an input to surface energy balance and hydrological models (Pettorelli et al. 2005b; Wang et al. 2020; Younes et al. 2019). Liu et al. (2019) performed FVC retrieval using GF-1/WFV and PMS based on the dimidiate pixel model and found that the uncertainty of PMS was lower than WFV due to higher spatial resolution. It demonstrates that more details about spatial soil/vegetation heterogeneity are beneficial for land degradation assessment. Sun et al. (2015) found that GF-1/WFV provided FVC with better accuracy than Landsat-8/OLI in sparse grassland ecosystems, and further reported that the correction of view angle effect resulting from large swath of GF-1/WFV could reduce uncertainty in the retrieval of the FVC by 7.5% - 7.8% with combination of HJ-1/CCD NDVI (Sun et al. 2020).

Deleted: ,

Zhang et al. (Zhang et al. 2013) retrieved FVC using VIs calculated from HJ-1/HSI data through an optimal band combination approach with good accuracy (R^2 = 0.86, RMSE = 0.11). Taking advantage of the high spatial and spectral resolutions of HJ-1/HSI, Liao & Zhang (2020) optimized the selection of endmember spectrum for theoretically pure vegetation, shaded, and soil based on Pixel Purity Index (PPI) and Endmember Average Root mean square error (EAR), and retrieved

FVC using the MESMA (Multiple Endmember Spectral Mixture Analysis) method. The results showed that, with the high spatial and spectral resolution data, the accuracy of the retrieved FVC was improved (RMSE = 0.19). Bian et al. (2017) proposed an adaptive Endmember Selection Linear Spectral Mixture Model (ASLSMM) based on HJ-1/CCD data to enhance the accuracy of FVC estimation. Compared with the traditional Linear Spectral Mixture Model (LSMM) and ~~Multiple Endmember Spectral Mixture Analysis (~~MESMA~~)~~ methods, the ASLSMM method is more consistent with the ground measurements. Liu et al. (2021) applied FY-3B/MERSI data to estimate FVC using PROSAIL vegetation radiative transfer model and random forest method, and the results showed good agreement with the EOLAB (Earth Observation Laboratory) reference FVC data (RMSE = 0.13).

3.3 Leaf Area Index

Leaf Area Index (LAI) refers to the total area of plant leaves per unit of land area (Chen and Black 1992), and is a key determinant of net primary productivity of ecosystems and energy exchange between the atmosphere and land surface (Wang et al. 2019a; Yan et al. 2019). Li et al. (2016) used a statistical regression approach to estimate LAI of winter wheat from HJ-1/CCD images with good accuracy (relative RSME, or rRMSE = 29.15%). Wei et al. (2017c) and Lei et al. (2018) applied the physical PROSAIL model to retrieve LAIs of maize crop and *Acacia Ricchii* plantation respectively using GF-1/WFV data, and reported similar accuracies (RMSE = 0.5 m^2 m^{-2} for maize crop, and RMSE = 0.13 m^2 m^{-2} for *Acacia Ricchii* plantation).

Commented [MX4]: 上边刚写过全称，这里不用再重复了。

Formatted: Strikethrough

Formatted: Strikethrough

Formatted: Strikethrough

Deleted: truth

Deleted: , and the inversion is efficient and accurate

Deleted: R

Formatted: Superscript

Formatted: Not Superscript/ Subscript

Formatted: Superscript

Formatted: Not Superscript/ Subscript

In addition to empirical and physical model-based approaches, machine learning (ML) has also been used to retrieve LAI from CEOS data. Lei et al. (2018) found ML-based approach offered higher accuracy (RMSE = 0.50 m^2 m^{-2}) in estimating LAI than the empirical VI-based regression approach (RMSE = 0.67 m^2 m^{-2}). Wei et al. (2017a) estimated LAIs of cropland from GF-5/AHSI hyperspectral data using the RF-KNN model with an RMSE of 0.70 m^2 m^{-2}.

3.4 Aboveground Biomass

Aboveground Biomass (AGB) refers to the total amount of plant-derived living and dead organic matter per unit of surface area, which is an important component of terrestrial carbon cycle. Obtaining the spatial and temporal variations of AGB with high accuracy is critical to many applications such as the estimation of crop yields, pasture forage and forest timber production (Brown et al. 1996; Lu 2006). Wang et al. (2014b) estimated the AGB of the Yellow River Estuary wetlands from GF-1/WFV data using statistical regression approach against ground samplint data with an MRE (Mean Relative Error) of 23.9%. Gou et al. (2019) combined VIs and texture information extracted from GF-2/PMS images to estimate the AGB of *Pinus tabuliformis* plantations with an RMSE of 0.43 t/hm^2 . Gao et al. (2019) retrieved AGB using high-resolution unmanned aerial vehicle (UAV) measurement, then scaled up to regional scale by establishing a regression model using GF-1/WFV NDVI. It reported that the uncertainty was reduced (RMSE = 68.04 g/m^2) in comparison to only using GF-1/WFV (RMSE = 128.75 g/m^2).

ZY-3/MUX data were also used for estimating AGB, such as in Gao et al. (2014), in which the

Formatted: Superscript
Formatted: Superscript
Formatted: Superscript
Commented [MX5]: 这个的全称介绍过了吗？
Formatted: Superscript
Deleted:
Deleted: estimation
Deleted: accuracy
Deleted: improved
Commented [MX6]: AGB 单位建议统一，要么用 t/hm^2，要么用 g/m^2，可以自己转换一下。
Deleted: that of the estimates by
Deleted:

regression model between VIs acquired from ZY-3/MUX and ground measured shrub AGB in mountainous areas was established. Due to the capability of acquiring multi-angle observations with the three TDI cameras, the stereo image can be obtained, from which detailed topographic information can be used to perform accurate topographic correction to the original data, leading to 1 21% reduction in the uncertainty in the estimated AGB. Taking the advantage of the multitemporal, high-resolution multispectral, and stereo images provided by ZY-3/TDI, Li et al. (2019a) proposed an improved workflow for estimating forest AGB based on the retrieval of relative canopy height, which produced AGB retrieval with higher accuracy (RMSE = 24.49 Mg/ha, rRMSE =21.37%) compared to the derived AGB using spectral data only (RMSE = 33.89 Mg/ha, rRMSE = 29.57%).

3.5 Sun-induced chlorophyll fluorescence (SIF)

Under the illumination of natural light, green plants can release the light at the wavelength of 650 - 800 nm during photosynthetic activity, which is named as Solar-Induced chlorophyll Fluorescence (SIF) (Joiner et al. 2013). SIF is the by-products of photosynthesis, which originated from Absorbed Photosynthetically Active Productivity (APAR) and has a common origin with plants' carbon sequestration and heat dissipation. Hence, SIF is highly related to vegetation stress conditions (Porcar-Castell et al. 2014), and has the potential to be a good remote sensing proxy for Gross Primary Productivity (GPP) (Guanter et al. 2014, Mohammed et al. 2019).

Previously, data sources used for retrieving SIF mainly include GOSAT, OCO-2, GOME-2, SCIAMACHY, and Sentinel-5P/TROPOMI (Joiner et al. 2011; Frankenberg et al. 2014; Köhler et

Deleted: improve the a

Deleted: ccuracy of

Deleted: by applying accurate topographic correction, leading to a decrease in SD (Standard Deviation) by 21.2%

Commented [MX7]: 单位统一

Deleted: R

Deleted: R

Deleted: Estimating sun-induced chlorophyll fluorescence (SIF) from remote sensing data is a rapidly advancing field in terrestrial vegetation science (Mohammed et al. 2019).

Deleted: In other words,

Deleted:).

Deleted:

al. 2015, 2018; Sun et al. 2018). Recently, the potential of estimating SIF and related GPP products (Du et al. 2021) from Chinese TanSat has also been explored. Du et al. (2018) used the TanSat data for retrieving global SIF, and the result agreed well with the pattern obtained from the OCO-2 SIF product (R^2=0.86), providing a new opportunity for global sampling of SIF at fine spatial resolution ($2\ km \times 2\ km$). Li et al. (2021) developed an approach for retrieving SIF from ultra-high spectral satellite data and tested using both TanSat and OCO-2 data. Ma et al. (2020) generated a Global Spatially Continuous TanSat SIF Product using the machine-learning method with a spatial resolution of $0.05°$, showing a good consistency with the TROPOMI SIF data ($R^2 = 0.73$). Yao et al. (2021) used TanSat data to produce a new global SIF product for 757 nm spanning the period of March, 2017 to February, 2018 based on the Institute of Atmospheric Physics Carbon Dioxide Retrieval Algorithm for Satellite Remote Sensing (IAPCAS)-DOAS method. In general, TanSat IAPCAS-DOAS/SIF product showed the seasonal variation of derived SIF being consistent with the vegetation growing state throughout the year, which has also been observed by the GOSAT and OCO-2 SIF products. Based on the above research, several global SIF products from TanSat have been developed and released for public access (Table 5).

Table 5 Global SIF products from TanSat

Author	Time Spanning	Temporal Resolution	Spatial Resolution	Links	Note
Liu et al.	2017.3-2019.8	1 day	2km	http://data.casearth.cn/sdo/detail/5d905086088716491c0cc1f4	Available
Du et al.	2017.7	1 day	2km	https://doi.org//10.13140/RG.2.2.14775.98726	Available
Ma et al.	2017.1-2019.12	4 days	0.05°	https://zenodo.org/record/3884309	Available

- **Deleted:** to obtain
- **Commented [MX8]:** 没必要用公式编辑器
- **Deleted:** RF-ML
- **Commented [MX9]:** 同上
- **Deleted:** 4
- **Deleted:** 4
- **Commented [MX10]:** 注意表格宽度
- **Field Code Changed**
- **Formatted:** No underline, Font colour: Auto
- **Formatted:** No underline, Font colour: Auto
- **Formatted:** No underline, Font colour: Auto
- **Field Code Changed**
- **Formatted:** No underline, Font colour: Auto
- **Formatted:** No underline, Font colour: Auto
- **Formatted:** No underline, Font colour: Auto
- **Field Code Changed**
- **Formatted:** No underline, Font colour: Auto
- **Formatted:** No underline, Font colour: Auto
- **Formatted:** No underline, Font colour: Auto

Yao et al.	2017.3-2018.2	unknown	2°	https://www.chinageoss.org/tansat	To be published

Formatted: No underline, Font colour: Auto

Field Code Changed

Formatted: No underline, Font colour: Auto

Formatted: No underline, Font colour: Auto

4 Research opportunities offered by the addition of CEOS sensors

4.1 Multi-sensor data fusion

Observations from a single satellite sensor often trade off spatial resolution against temporal resolution, or vice versa, resulting in sub-optimal resolving capability for monitoring vegetation dynamics. It is an effective way for achieving both high spatial and temporal resolutions by fusing data from different sensors. Pi et al. (2021) reconstructed an NDVI dataset with 16 m spatial resolution and 16-day temporal resolution by fusing GF-1/WFV with MOD13Q1 NDVI based on the STARFM (Spatial and Temporal Adaptive Reflectance Fusion Model) algorithm. Yin et al. (2016) found that by fusing EOS/MODIS and FY-3/MERSI observations, which share high similarity in terms of spectral band configuration, the spatio-temporal gaps of LAI retrievals were significantly reduced, leading to more complete data over the cloud-prone sub-tropical and tropical forests. Wu et al. (2015) applied the Spatial and Temporal Data Fusion Approach (STDFA) to create a time series daily NDVI for crop phenology monitoring through the fusion of HJ-1/CCD or GF-1/WFV with MODIS data, and the output revealed detailed sub-field crop growth at daily time-step. Refined spatio-temporal resolutions by multi-sensor fusion would offer many advantages to applications such as habitat quality assessment, crop yield prediction, as well as urban phenology

Deleted: monitoring

Deleted: of

Deleted: valid

Deleted: many

research.

4.2 Data continuity & data recovery

For global change studies, it is critical to ensure long-term data continuity and consistency. China has launched and is planning to launch many spaceborne sensors covering a wide range of sensor types and spatial-temporal resolutions, offering great potential to achieve sustainable monitoring of global change, or be used as a backup for other commonly used sensors. For instance, the hyperspectral instrument AHSI onboard the CEOS GF-5 with 30 m spatial resolution and 330 narrow spectral bands, together with ASI/PRISMA and DLR/DESIS, can be good successors for the EO-1/Hyperion which has ceased operation since 2014.

On other occasions, orbiting sensor is possible to encounter instrument failure. If similar instruments are available from other satellites, a virtual constellation can be formed to mimic the functioning (He et al. 2018; Yueh et al. 2016). One example is the recovery of the SMAP mission after the radar failure by ingesting data from ESA's Sentinel-1 C-band SAR (Meyer et al. 2021), and in this case GF-3 C-band SAR can be an alternative. Another example is filling the data gaps caused by the Scan-Line-Corrector off (SLC-off) failure of Landsat-7/ETM+ using Sentinel-2/MSI (Wang et al. 2021). HJ-1/CCD has the same spatial resolution and almost identical band configuration with Landsat-7/ETM, and hence its potential for resolving the SLC-off issue can also be explored in the future (Figure 3). These are all beneficial to the end-users in global vegetation and ecological remote sensing community.

Deleted: of long-term data

Deleted: new

Deleted: loaded on

Deleted:

Deleted: . In addition

Deleted: ,

Deleted: is also an alternative to the radar in SMAP missions…

Deleted: . It

Deleted: provides seamless imagery that greatly improves the related scientific research and applications. Besides, the

Deleted:

Deleted: that started operating from 2009 is also able to be the successo

Deleted: r of ETM+ since they have the same spatial resolution and almost identical band configuration

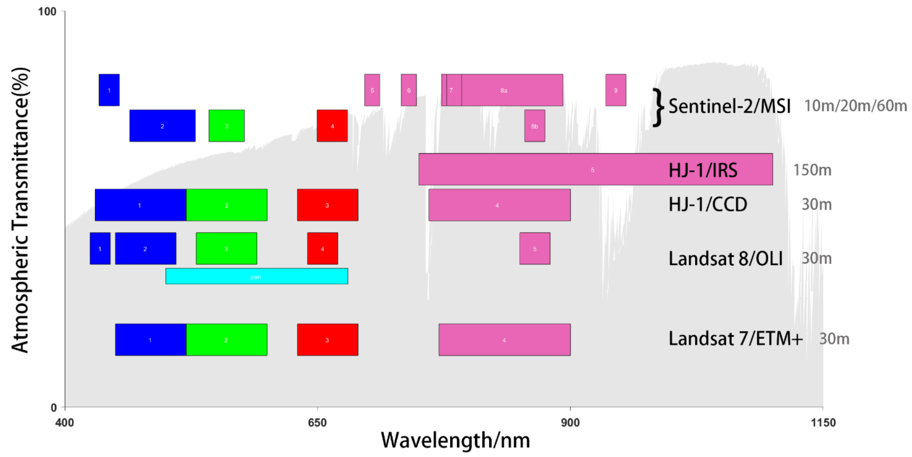

Figure 3 Spectral band comparisons among Landsat-7/ETM+, Landsat-8/OLI, HJ-1/CCD, HJ-1/IRS, and Sentinel-2/MSI

Deleted:

4.3 Multi-angle remote sensing

Multi-angle remote sensing is an effective way to infer surface BRDF (Bidirectional Reflectance Distribution Function) that can be further used to retrieve albedo, normalize surface reflectance anisotropy and estimate vegetation structure (Yan et al. 2021). BRDF retrieval using single-sensor data often suffers from limited angular sampling due to cloud or aerosols, e.g. MODIS has only a 75.8% probability that having more than 7 cloud-free observations within a 16 d window (Wen 2015). Multi-sensor data can be combined to accumulate a sufficient number of multi-angle observations in a short time for improving BRDF retrievals. In addition, multi-angle data can also be used to improve the retrievals of vegetation parameters. Bicheron et al. (1999) reported that forest classification uncertainty can be reduced if multi-spectral data is used in conjunction with multi-angle data which can provide additional information about forest canopy structure (Hyman

Deleted: ,

and Barnsley 1997). Wen et al. (2016) developed a multi-sensor combined BRDF inversion (MCBI) by combining data from MODIS, AVHRR, VIIRS and FY-3/MERSI, and shortened the retrieval window up to 4 days in comparison to the standard 16-day product by only using MODIS data. Sensors onboard the CEOSs, in together with other spaceborne sensors, can offer great potential for obtaining multi-angle data via rigorous cross-sensor calibration.

5 Concluding remarks

China has invested immensely in EO missions over the past decade, creating now a spaceship fleet resembling those from NASA or ESA. It has been demonstrated by the recent studies that the sensors onboard the CEOSs performed generally well in remote sensing of vegetation applications. These sensors can be used either solely for retrieving vegetation parameters or in together with other international satellites for multi-sensor applications. Although most applications we reviewed here were mainly performed by the Chinese research community, the international users are certainly encouraged to access the data as most of the data we reviewed above are publicly available and have English language support for the data access portal. The experiences and critics gain from both the domestic and international end-users would be extremely valuable to the CEOS programs to further improve sensors quality and reliability, eventually leading to a better understanding of pressing scientific issues such as global environmental change, sustainability development, food security and biodiversity conservation. While this article is being read, CEOS sensors are continuously measuring reflectance and echo over the entire planet. It is now the time to capitalize

Deleted: encompassing a full-suite of sensors to some extent

Deleted: the fleet

Deleted: ,

Deleted: , JAXA and other major space agencies

Deleted: Driven by the application requirements, China has launched and is planning to launch more satellites carrying sensors equivalent to or even better than those past sensors. Since more CEOS satellites are launched, more studies that attempt to use or integrate CEOS data are encouraged to use CEOS data for vegetation and ecological remote sensing.

Deleted: data p

Deleted: the estimation of vegetation parameters with high spatial and temporal resolutions,

Deleted: and even help to improve the continuity and validity of earth observations by combining them with remote sensing data from other international earth observation missions

Deleted: Now

Deleted: as

Deleted: are

Deleted: also

Deleted: (with user registration sometimes required)

Deleted: webpage

Deleted: in English language

Deleted: valuable

Deleted: in turn be used to

Deleted: all aspects of CEOS

Deleted: and

them for the benefit of global vegetation and Earth monitoring.

Deleted:

Acknowledgement

This study is supported by National Natural Science Foundation of China (No. 42171305, Principal Investigator: X. Ma); Natural Science Foundation of Gansu Province, China (No. 21JR7RA499, PI: X. Ma); Fundamental Research Funds for the Central Universities (No. lzujbky-2021-ct11, PI: X. Ma). The authors thank Yifei Gao for preparing reference list.

Deleted:

Appendix

Table A1 Comparison between GF-1(6)/WFV and Sentinel-2/MSI

Satellite	Payload	Band No.	Spectral Range (μm)	Spatial Resolution at nadir (m)	Swath Width (km)	Revisit Cycle (days)
GF-1	Wide-Field View Multispectral Camera (WFV)	1	0.45~0.52	16	800 (4 Cameras)	2
		2	0.52~0.59			
		3	0.63~0.69			
		4	0.77~0.89			
GF-6		1	0.45~0.52	16		
		2	0.52~0.59			
		3	0.63~0.69			
		4	0.77~0.89			
		5	0.69~0.73			
		6	0.73~0.77			
		7	0.40~0.45			
		8	0.59~0.63			
Sentinel-2	Multi-Spectral Instrument (MSI)	2	0.458~0.523	10	290	5
		3	0.543~0.578			
		4	0.65~0.68			
		8	0.785~0.90			
		5	0.698~0.713	20		

Deleted: Sensor

Deleted: with

		6	0.733~0.748	
		7	0.773~0.793	
		8A	0.855~0.875	
		11	1.565~1.655	
		12	2.10~2.28	
		1	0.433~0.453	
		9	0.935~0.955	60
		10	1.365~1.385	

Table A2 Comparison between GF-1(6)/PMS, ZY-3/MUX and SPOT-6(7)/NAOMI

Satellite	Payload	Band No.	Spectral Range (μm)	Spatial Resolution at nadir (m)	Swath Width (km)	Revisit Cycle (days)
GF-1/6	Panchromatic & Multispectral Camera (PMS)	pan	0.45~0.90	2	60 (2 Cameras)	4
		1	0.45~0.52	8		
		2	0.52~0.59			
		3	0.63~0.69			
		4	0.77~0.89			
ZY-3	Multispectral Camera (MUX)	1	0.45~0.52	6	51	5
		2	0.52~0.59			
		3	0.63~0.69			
		4	0.77~0.89			
SPOT-6/7	New Astrosat Optical Modular Instrument (NAOMI)	pan	0.45~0.75	1.5	60	1 (2 Cameras)
		1	0.45~0.52	6		
		2	0.53~0.6			
		3	0.62~0.69			
		4	0.76~0.89			

Deleted: Sensor

Deleted: with

Deleted: with

Table A3 Comparison between GF-2/PMS, QuickBird and WorldView-3/WV110

Satellite	Payload	Band No.

Deleted: Sensor

			Spectral Range (μm)	Spatial Resolution at nadir (m)	Swath Width (km)	Revisit Cycle (days)
GF-2	Panchromatic & Multispectral Camera (PMS)	pan	0.45~0.90	1	45(with 2 Cameras operating simultaneously)	5
		1	0.45~0.52	4		
		2	0.52~0.59			
		3	0.63~0.69			
		4	0.77~0.89			
QuickBird	State-of-the-Art BGIS 2000 Sensor	pan	0.45~0.90	0.65	16.8/18-Early 2013	1-3.5 days
		1	0.45~0.52	2.62		
		2	0.52~0.60			
		3	0.63~0.69			
		4	0.76~0.90			
WorldView Satellites(-3)	WorldView-110 camera (WV110)	pan	0.45-0.80	0.31	13.1	1(4.5) day(s) at 1(0.59)-metre GSD resolution
		1	0.40~0.45	1.24		
		2	0.45~0.51			
		3	0.51~0.58			
		4	0.585~0.625			
		5	0.63~0.69			
		6	0.705~0.745			
		7	0.77~0.895			
		8	0.86~1.04			
		8 SWIR bands	1.195~2.365	3.7		
		12 CAVIS bands	0.405~2.245	30		

Table A4 Comparison of SAR satellites between GF-3 and Sentinel-1

Satellite	Payload	Operational Mode	Spatial Resolution at nadir (m)	Swath Width (km)	Polarization Mode (Selectable)

Deleted: Sensor

GF-3	C-band Synthetic Aperture Radar (SAR)	SL	1	10	single-polarization
		UFS	3	30	single-polarization
		FS1	5	50	dual-polarization
		FS2	10	100	dual-polarization
		SS	25	130	dual-polarization
		NSC	50	300	dual-polarization
		WSC	100	500	dual-polarization
		QPS1	8	30	full polarization
		QPS2	25	40	full polarization
		WAVE	10	5	full polarization
		GLOGAL	500	650	dual-polarization
		EXTENDED1	25	130	dual-polarization
		EXTENDED2	25	80	dual-polarization
Sentinel-1	C-band Synthetic Aperture Radar (SAR)	SM	5	80	full polarization
		IW	5×20	250	full polarization
		EW	25×100	400	full polarization
		WV	5×20	20	single-polarization

Table A5 Comparison of Hyperspectral satellites between GF-5/AHSI, HJ-1A/HSI, DLR/DESIS and PRISM

Deleted: HIS

Satellite	Payload	Number of Bands	Spectral Range (μm)	Spectral Resolution(nm)	Spatial Resolution at nadir (m)	Swath Width (km)	Revisit Cycle (days)
HJ-1A	Hyperspectral Imager (HSI)	110-128	0.45~0.95	3.9~4.5	100	50	4
GF-5	Advanced Hyperspectral Imager (AHSI)	300	0.40~2.50	5(VNIR) 10(SWIR)	30	60	5
DLR	DLR Earth Sensing	235	0.40~1.00	2.55	30	30	3-5

Deleted: Sensor

	Imaging Spectrometer (DESIS)						
PRISMA	-	240	0.40~2.50	< 12	30	30	7

Table A6 Comparison of TanSat/ACGS, OCO-2 and Sentinel-5P/TROPOMI

Satellite	Payload	Band No.	Spectral Range (nm)	Spectral Resolution (nm)	Spatial Resolution (km)	Swath Width (km)	Revisit Cycle (days)
TanSat	Atmospheric Carbon-dioxide Grating Spectroradiometer (ACGS)	$O_2 - A$	758~778	0.033-0.047	2	20	16
OCO-2	Spectrometers	$O_2 - A$	758~772	0.04	1.29×2.25	10.6	16
Sentinel-5P	TROPOspheric Monitoring Instrument (TROPOMI)	NIR	675~775	0.5	7×7	2600	1

Deleted: Sensor

References

Aplin, P. (2005). Remote sensing: ecology. Progress in Physical Geography, 104-113

Deleted: :

Bannari, A., Morin, D., Bonn, F., & Huete, A. (1995). A review of vegetation indices. Remote sensing reviews, 13, 95-120

Bian, J.H., Li, A.N., Zhang, Z.J., Zhao, W., Lei, G.B., Yin, G.F., Jin, H.A., Tan, J.B., & Huang, C.Q. (2017). Monitoring fractional green vegetation cover dynamics over a seasonally inundated alpine wetland using dense time series HJ-1A/B constellation images and an adaptive endmember selection LSMM model. Remote Sensing of Environment, 197, 98-114

Bicheron, P., & Marc, L. (1999). A method of biophysical parameter retrieval at global scale by inversion of a vegetation reflectance model. Remote Sensing of Environment, 1999, 251-266

Brown, S., Sathaye, J.A., & Kauppi, P. (1996). Mitigation of carbon emissions to the atmosphere by forest management. Commonwealth Forestry Review

Chen, J.M., & Black, T.A. (1992). Defining Leaf-Area Index for Non-Flat Leaves. Plant Cell and Environment, 15, 421-429

Chen, X., & Liu, Z. (2015). Quantitative Analysis of Relationship Between HJ-1NDVI and MODIS NDVI. Remote Sensing Information

Cohen, W.B., & Goward, S.N. (2004). Landsat's role in ecological applications of remote sensing. BioScience, 54, 535-545

Davis, C.L., Hoffman, M.T., & Roberts, W. (2017). Long-term trends in vegetation phenology and productivity over Namaqualand using the GIMMS AVHRR NDVI3g data from 1982 to 2011. South African Journal of Botany, 111, 76-85

Dong, C.H., Yang, J., Zhang, W.J., Yang, Z.D., Lu, N.M., Shi, J.M., Zhang, P., Liu, Y.J., & Cai, B. (2009). An Overview of a New Chinese Weather Satellite FY-3A. Bulletin of the American Meteorological Society, 90, 1531

Du, S., Liu, L., Liu, X., & Chen, J. (2021). First Investigation of the Relationship Between Solar-Induced Chlorophyll Fluorescence Observed by TanSat and Gross Primary Productivity. IEEE Journal of Selected Topics in Applied Earth Observations and Remote Sensing, 14, 11892-11902

Du, S., Liu, L., Liu, X., Zhang, X., Zhang, X., Bi, Y., & Zhang, L. (2018). Retrieval of global terrestrial solar-induced chlorophyll fluorescence from TanSat satellite. Science Bulletin, 63, 1502-1512

Feng, L., Guo, S., Zhu, L.J., Fang, X.Q., & Zhou, Y.A. (2017). Urban vegetation phenology analysis and the response to the temperature change. 2017 Ieee International Geoscience and Remote Sensing Symposium (Igarss), 5743-5746

Frankenberg, C., O'Dell, C., Berry, J., Guanter, L., Joiner, J., Köhler, P., Pollock, R., & Taylor, T.E. (2014). Prospects for chlorophyll fluorescence remote sensing from the Orbiting Carbon Observatory-2. Remote Sensing of Environment, 147, 1-12

Gao, M.L., Zhao, W.J., Gong, Z.N., Gong, H.L., Chen, Z., & Tang, X.M. (2014). Topographic Correction of ZY-3 Satellite Images and Its Effects on Estimation of Shrub Leaf Biomass in Mountainous Areas. Remote Sensing, 6, 2745-2764

Gao, Y., Liang, Z., Wang, B., Wu, Y., & Liu, S. (2019). UAV and satellite remote sensing images based aboveground biomass inversion in the meadows of Lake Shengjin. Journal of Lake Sciences, 31, 517-528

Ge, M., Zhao, J., Zhong, B., & Yang, A. (2017). Comparison of the Vegetation Indexes between FY-3/VIRR,FY-3/MERSI and EOS/MODIS Data. Remote Sensing Technology and Application, 32, 12

Gianelle, D., Vescovo, L., & Mason, F. (2009). Estimation of grassland biophysical parameters using hyperspectral reflectance for fire risk map prediction. International journal of wildland fire, 18, 815-824

Gitelson, A.A., Kaufman, Y.J., Stark, R., & Rundquist, D. (2002). Novel algorithms for remote estimation of vegetation fraction. Remote Sensing of Environment, 80, 76-87

Gou, R., Chen, J., Duan, G., Yang, R., Bu, Y., Zhao, J., & Zhao, P. (2019). Inversion of aboveground biomass of Pinus tabuliformis plantations based on GF-2 data. Chinese Journal of Applied Ecology, 30, 4031-4040

He, L., Hong, Y., Wu, X., Ye, N., Walker, J.P., & Chen, X. (2018). Investigation of SMAP Active–Passive Downscaling Algorithms Using Combined Sentinel-1 SAR and SMAP Radiometer Data. IEEE Transactions on Geoscience and Remote Sensing, 56, 4906-4918

Huang, W., Sun, S.R., Jiang, H.B., Gao, C., & Zong, X.Y. (2018). GF-2 Satellite 1m/4m Camera Design and In-Orbit Commissioning. Chinese Journal of Electronics, 27, 1316-1321

Hyman, A.H., & Barnsley, M.J. (1997). On the potential for land cover mapping from multiple-view-angle (MVA) remotely-sensed images. International Journal of Remote Sensing, 18, 2471-2475

Ji, M., Tang, B., & Li, Z. (2019). Review of Solar-induced Chlorophyll Fluorescence Retrieval Methodsfrom Satellite Data. Remote Sensing Technol. Appl, 3, 455-466

Joiner, J., Yoshida, Y., Vasilkov, A.P., Yoshida, Y., Corp, L.A., & Middleton, E.M. (2011). First observations of global and seasonal terrestrial chlorophyll fluorescence from space. Biogeosciences, 8, 637-651

Kalaitzidis, C., Heinzel, V., & Zianis, D. (2010). A review of multispectral vegetation indices for biomass estimation. In, Proceedings of the 29th symposium of the European association of remote sensing laboratories, Chania, Greece. IOS Press Ebook (pp. 201-208)

Kerr, J.T., & Ostrovsky, M. (2003). From space to species: ecological applications for remote sensing. Trends in Ecology & Evolution, 18, 299-305

Köhler, P., Guanter, L., & Joiner, J. (2015). A linear method for the retrieval of sun-induced chlorophyll fluorescence from GOME-2 and SCIAMACHY data. Atmospheric Measurement Techniques, 8, 2589-2608

Köhler, P., Guanter, L., Kobayashi, H., Walther, S., & Yang, W. (2018). Assessing the potential of sun-induced fluorescence and the canopy scattering coefficient to track large-scale vegetation dynamics in Amazon forests. Remote Sensing of Environment, 204, 769-785

Lei, Y., Zhu, S., Guo, Y., Li, D., Liu, L., & Liu, N. (2018). Inversion of Leaf Area Index Based on Extreme Learning Machine Regression in Road Vegetation. Bulletin of Surveying and Mapping, 5

Li, D. (2012). China's First Civilian Three-line-array Stereo Mapping Satellite: ZY-3 Acta Geodaetica et Cartographica Sinica, 41, 317-322

Li, F., Song, G., Liujun, Z., Xiuqin, F., & Yanan, Z. (2017). Urban vegetation phenology analysis and the response to the temperature change. In, 2017 IEEE International Geoscience and Remote Sensing Symposium (IGARSS) (pp. 5743-5746): IEEE

Li, G.Y., Xie, Z.L., Jiang, X.D., Lu, D.S., & Chen, E.X. (2019a). Integration of ZiYuan-3 Multispectral and Stereo Data for Modeling Aboveground Biomass of Larch Plantations in North China. Remote Sensing, 11

Li, H., Chen, Z.X., Jiang, Z.W., Wu, W.B., Ren, J.Q., Liu, B., & Hasi, T. (2017). Comparative analysis of GF-1, HJ-1, and Landsat-8 data for estimating the leaf area index of winter wheat. Journal of Integrative Agriculture, 16, 266-285

Li, H., Peng, R., Li, W., Zhu, X., Huang, Y., & Nie, Q. (2019 b). Filtering algorithms of HJ-1 A/B NDVI time series data and phenology of typical tree species in Xiamen. Chinese Journal of Ecology

Li, S., Gao, M., Li, Z.-L., Duan, S., & Leng, P. (2021a). Uncertainty analysis of SVD-based spaceborne far–red sun-induced chlorophyll fluorescence retrieval using TanSat satellite data. International Journal of Applied Earth Observation and Geoinformation, 103

Li, S., Gao, M., & Li, Z.L. (2021b). Retrieving Sun-Induced Chlorophyll Fluorescence from Hyperspectral Data with TanSat Satellite. Sensors (Basel), 21

Li, X., Zhang, Y., Luo, J., Jin, X., Xu, Y., & Yang, W. (2016). Quantification winter wheat LAI with HJ-1CCD image features over multiple growing seasons. International Journal of Applied Earth Observation and Geoinformation, 44, 104-112

Liu, D.Y., Jia, K., Jiang, H.Y., Xia, M., Tao, G.F., Wang, B., Chen, Z.L., Yuan, B., & Li, J. (2021). Fractional Vegetation Cover Estimation Algorithm for FY-3B Reflectance Data Based on Random Forest Regression Method. Remote Sensing, 13

Liu, R., Ren, H., Liu, S., Liu, Q., Yan, B., & Gan, F. (2018). Generalized FPAR estimation methods from various satellite sensors and validation. Agricultural and Forest Meteorology, 260, 55-72

Liu, Y., Wang, J., Yao, L., Chen, X., Cai, Z., Yang, D., Yin, Z., Gu, S., Tian, L., Lu, N., & Lyu, D. (2018). The TanSat mission: preliminary global observations. Science Bulletin, 63, 1200-1207

Liu, Z., Mo, R., Sun, X., & Lv, X. (2019). Analysis of Influence of GFn-1 Data Resolution on Extraction of Vegetation Coverage Information. Rural Economy and Science-Technology, 30, 80-82

Lu, D. (2006). The potential and challenge of remote sensing-based biomass estimation. International Journal of Remote Sensing, 27, 1297-1328

Ma, Y., Liu, L., Chen, R., Du, S., & Liu, X. (2020). Generation of a Global Spatially Continuous TanSat Solar-Induced Chlorophyll Fluorescence Product by Considering the Impact of the Solar Radiation Intensity. Remote Sensing, 12

Mancino, G., Ferrara, A., Padula, A., & Nolè, A. (2020). Cross-Comparison between Landsat 8 (OLI) and Landsat 7 (ETM+) Derived Vegetation Indices in a Mediterranean Environment. Remote Sensing, 12

Meyer R, Zhang W, Kragh S J, et al. Exploring the combined use of SMAP and Sentinel-1 data for downscaling soil moisture beyond the 1 km scale[J]. Hydrology and Earth System Sciences Discussions, 2021: 1-25.

Nara, H., & Sawada, Y. (2021). Global Change in Terrestrial Ecosystem Detected by Fusion of Microwave and Optical Satellite Observations. Remote Sensing, 13

Pan, T. (2015). Technical Characteristics of GF-2 Satellite. Aerospace China, 3-9

Pettorelli, N. (2013). The normalized difference vegetation index. Oxford University Press

Pettorelli, N., Vik, J.O., Mysterud, A., Gaillard, J.-M., Tucker, C.J., & Stenseth, N.C. (2005). Using the satellite-derived NDVI to assess ecological responses to environmental change. Trends in ecology & evolution, 20, 503-510

Pi, X., Zeng, Y., & He, C. (2021). Estimating urban vegetation coverage on the basis of multi-source remote sensing data and temporal mixture analysis. Journal of Remote Sensing, 25, 1216-1226

Ran, Y., & Li, X. (2019). TanSat: a new star in global carbon monitoring from China. Science Bulletin, 64, 284-285

Song, D., Wang, Z., Li, Y., & Hu, Y. (2018). Cropland Phenology Detection Based on HJ-1A/B CCD Data in Jianghan Plain. Geomatics & Spatial Information Technology, 41, 5

Sun, Y., Frankenberg, C., Jung, M., Joiner, J., Guanter, L., Köhler, P., & Magney, T. (2018). Overview of Solar-Induced chlorophyll Fluorescence (SIF) from the Orbiting Carbon Observatory-2: Retrieval, cross-mission comparison, and global monitoring for GPP. Remote Sensing of Environment, 209, 808-823

Sun, Z., Liu, S., Jiang, J., Bai, X., Chen, Y., Zhu, C., & Guo, W. (2017). Coordination inversion methods for vegetation cover of winter wheat by multi-source satellite images. Transactions of the Chinese Society of Agricultural Engineering, 33, 7

Tang, X., & Hu, F. (2018). Development Status and Trend of Satellite Mapping. Spacecraft Recovery & Remote Sensing, 39, 26-35

Wang, J., Li, X., & Fan, W. (2014a). Monitoring Vegetation Phenology Using HJ-CCD Image of High and Moderate Resolution Remote Sensing Data:A Case Study in Upper Stream of Miyun Reservoir. Journal of Northeast Forestry University, 88-94

Wang, J., Zhang, J., Ma, Y., & Ren, G. (2014b). Study on the Above Ground Vegetation Biomass Estimation Model Based on GF-1 WFV Satellite Image in the Yellow River Estuary Wetland. Acta Laser Biology Sinica, 604-608

Wang, Q., Wang, L., Wei, C., Jin, Y., Li, Z., Tong, X., & Atkinson, P.M. (2021). Filling gaps in Landsat ETM+ SLC-off images with Sentinel-2 MSI images. International Journal of Applied Earth Observation and Geoinformation, 101

Wang, S., Zhang, B., Zhai, X., & Sun, H.-l. (2020). Vegetation cover changes and sand-fixing service responses in the Beijing–Tianjin sandstorm source control project area. Environmental Development, 34, 100455

Wang, Y.C., Liu, Y.X., Li, M.C., & Tan, L. (2014). The reconstruction of abnormal segments in HJ-1A/B NDVI time series using MODIS: a statistical method. International Journal of Remote Sensing, 35, 7991-8007

Wang, Z.Z., Li, J.Y., He, J.Y., Zhang, S.W., Gu, S.Y., Li, Y., Guo, Y., & He, B.Y. (2019). Performance Analysis of Microwave Humidity and Temperature Sounder Onboard the FY-3D Satellite From Prelaunch Multiangle Calibration Data in Thermal/Vacuum Test. IEEE Transactions on Geoscience and Remote Sensing, 57, 1664-1683

Wei, X., Gu, X., Meng, Q., Yu, T., Zhou, X., Wei, Z., Jia, K., & Wang, C. (2017a). Leaf Area Index Estimation Using Chinese GF-1 Wide Field View Data in an Agriculture Region. Sensors (Basel), 17

Wei, X.Q., Gu, X.F., Meng, Q.Y., Yu, T., Jia, K., Zhan, Y.L., & Wang, C.M. (2017b). Cross-Comparative Analysis of GF-1 Wide Field View and Landsat-7 Enhanced Thematic Mapper Plus Data. Journal of Applied Spectroscopy, 84, 829-836

Wei, X.Q., Gu, X.F., Meng, Q.Y., Yu, T., Zhou, X., Wei, Z., Jia, K., & Wang, C.M. (2017c). Leaf Area Index Estimation Using Chinese GF-1 Wide Field View Data in an Agriculture Region. Sensors, 17

Wen, J. (2015). Remote Sensing Modeling and Albedo Inversion of Land Surface Bidirectional Reflectance Characteristics. Science Press

Wen J, Dou B, You D, et al. Forward a small-timescale BRDF/Albedo by multisensor combined brdf inversion model[J]. IEEE Transactions on Geoscience and Remote Sensing, 2016, 55(2): 683-697.

Wu, M.Q., Zhang, X.Y., Huang, W.J., Niu, Z., Wang, C.Y., Li, W., & Hao, P.Y. (2015). Reconstruction of Daily 30 m Data from HJ CCD, GF-1 WFV, Landsat, and MODIS Data for Crop Monitoring. Remote Sensing, 7, 16293-16314

Wu, P., Hu, L., Li, G., Feng, Z., & Chen, C. (2011). Relationship between FY-3A/MERSI and MODIS Vegetation Indexes Based on Cotton Spectrum. Desert and Oasis Meteorology, 5, 4

Wulder, M.A., Hall, R.J., Coops, N.C., & Franklin, S.E. (2004). High spatial resolution remotely sensed data for ecosystem characterization. BioScience, 54, 511-521

Yao, L., Yang, D., Liu, Y., Wang, J., Liu, L., Du, S., Cai, Z., Lu, N., Lyu, D., Wang, M., Yin, Z., & Zheng, Y. (2021). A New Global Solar-induced Chlorophyll Fluorescence (SIF) Data Product from TanSat Measurements. Advances in Atmospheric Sciences, 38, 341-345

Yan, G., Hu, R., Luo, J., Weiss, M., Jiang, H., Mu, X., Xie, D., & Zhang, W. (2019). Review of indirect optical measurements of leaf area index: Recent advances, challenges, and perspectives. Agricultural and Forest Meteorology, 265, 390-411

Yan, G., Jiang, H., Yan, K., Cheng, S., Song, W., Tong, Y., Liu, Y., Qi, J., Mu, X., Zhang, W., Xie, D., & zhou, H. (2021). Review of optical multi-angle quantitative remote sensing. National Remote Sensing Bulletin, 25, 83-108

Yang, Z., Shao, Y., Li, K., Liu, Q., Liu, L., & Brisco, B. (2017). An improved scheme for rice phenology estimation based on time-series multispectral HJ-1A/B and polarimetric RADARSAT-2 data. Remote Sensing of Environment, 195, 184-201

Yin, G., Li, J., Liu, Q., Zhong, B., & Li, A. (2016). Improving LAI spatio-temporal continuity using a combination of MODIS and MERSI data. Remote Sensing Letters, 7, 771-780

Younes, N., Joyce, K.E., Northfield, T.D., & Maier, S.W. (2019). The effects of water depth on estimating Fractional Vegetation Cover in mangrove forests. International Journal of Applied Earth Observation and Geoinformation, 83

Yuan, Z., Yang, A., & Zhong, B. (2015). Cross comparison of the vegetation indexes between Landsat TM and HJ CCD. Remote Sensing for Land & Resources, 27, 5

Yueh, S., Entekhabi, D., O'Neill, P., Njoku, E., & Entin, J. (2016). NASA soil moisture active passive mission status and science performance. 2016 IEEE International Geoscience and Remote Sensing Symposium (IGARSS)

Zhang, L., Wang, S., & Huang, C. (2018). Top-of-atmosphere hyperspectral remote sensing of solar-induced chlorophyll fluorescence: A review of methods. Remote Sens, 22, 1-12

Zhang, X., Zhou, M., Wang, W., & Li, X. (2015). Progress of global satellite remote sensing of atmospheric compositions and its' applications. Science & Technology Review, 33, 13-22

Zhang, X.F., Liao, C.H., Li, J., & Sun, Q. (2013). Fractional vegetation cover estimation in arid and semi-arid environments using HJ-1 satellite hyperspectral data. International Journal of Applied Earth Observation and Geoinformation, 21, 506-512

Zhang, Y., Song, C., Band, L.E., Sun, G., & Li, J. (2017). Reanalysis of global terrestrial vegetation trends from MODIS products: Browning or greening? Remote Sensing of Environment, 191, 145-155

Zhao, B., Wang, H., & Zhang, A. (2019). Inter-sensor comparison and quantitative relationships between GF-1 WFV and Landsat 8 OLI NDVI data. Journal of Geomatics, 44, 6

Zhao, J., Li, J., Liu, Q., Wang, H., Chen, C., Xu, B., & Wu, S. (2018). Comparative Analysis of Chinese HJ-1 CCD, GF-1 WFV and ZY-3 MUX Sensor Data for Leaf Area Index Estimations for Maize. Remote Sensing, 10

Zhao, K., Xu, J., Zhao, Z., Song, L., & Xiao, K. (2013). Cross Comparison of HJ-1A/B CCD and Landsat TM/ETM+ Multispectral Measurements for NDVI, SAVI and EVI Vegetation Index. Remote Sensing Technology and Application, 28, 8

Zhao, L., Zhang, R., Liu, Y., & Zhu, X. (2020). The differences between extracting vegetation information from GF1-WFV and Landsat8-OLI. Acta Ecologica Sinica, 40, 12

Zhou, X., Yamaguchi, Y., & Arjasakusuma, S. (2018). Distinguishing the vegetation dynamics induced by anthropogenic factors using vegetation optical depth and AVHRR NDVI: A cross-border study on the Mongolian Plateau. Sci Total Environ, 616-617, 730-743

Zoungrana, B.J.B., Conrad, C., Thiel, M., Amekudzi, L.K., & Da, E.D. (2018). MODIS NDVI trends and fractional land cover change for improved assessments of vegetation degradation in Burkina Faso, West Africa. Journal of Arid Environments, 153, 66-75

Rahman, A. F., Sims, D. A., Cordove, V. D., El-Marsri, B. Z. (2005). Potential of MODIS EVI and surface temperature for directly estimating per-pixel ecosystem C fluxes. Geophysical Research Letters, 32(19), L19404.